FlatChem 20 (2020) 100152

Contents lists available at ScienceDirect

FlatChem

journal homepage: www.elsevier.com/locate/flatc

2D black TiO_{2-x} nanoplate-decorated Ti_3C_2 MXene hybrids for ultrafast and elevated stable lithium storage

Lin Sun[a,b], Jie Xie[a,c], Lei Zhang[a], Ruiyu Jiang[a,*], Jun Wu[a,*], Lele Fan[a], Rong Shao[a], Zhidong Chen[c], Zhong Jin[a,b,*]

[a] School of Chemistry and Chemical Engineering, Yancheng Institute of Technology, Yancheng 224051, PR China
[b] Key Laboratory of Mesoscopic Chemistry of MOE, State Key Laboratory of Coordination Chemistry, and Department of Chemistry and Chemical Engineering, Nanjing University, Nanjing 210023, PR China
[c] School of Petrochemical Engineering, Jiangsu Province Cultivation Base for State Key Laboratory of Photovoltaic Science and Technology, Changzhou University, Changzhou 213164, PR China

ARTICLE INFO

Keywords:
Lithium ion battery
Anode material
Hybrid material
MXene
TiO_{2-x}

ABSTRACT

Novel 2D black TiO_{2-x} nanoplate-decorated Ti_3C_2 MXene (TiO_{2-x}/Ti_3C_2) hybrids were rationally designed and prepared by a facile wet process. The MXene nanosheets, serving as the carriers, not only enable the rapid electron and ion transport at the interface, but also avoid the aggregation of TiO_{2-x} nanoplate during lithiation and de-lithiation. On the other hand, the presence of TiO_{2-x} nanoplate also acts as the spacer to avert the MXene nanosheets from severe restacking. The successful formation of TiO_{2-x}/Ti_3C_2 were examined by X-ray diffraction (XRD) analysis, fourier transform infrared spectroscopy (FT-IR), scanning electron spectroscopy (SEM), transmission electron spectroscopy (TEM) and X-ray photoelectron spectroscopy (XPS). When served as anodes in lithium ion batteries (LIBs), the resulting TiO_{2-x}/Ti_3C_2 hybrid electrode delivers high specific capacity of 131 mA h g^{-1} even cycling at a high current density of 5 A g^{-1} (17 C) for 500 times and superior rate capability (even at a current density of 34 C, the specific capacity still remains at 115 mA h g^{-1}), which highlight its great promise in the fields of energy storage and conversion.

1. Introduction

Lithium ion batteries (LIBs) represent a cutting-edge energy storage technology for storing variable energies such as solar and wind energy, and are efficient and sentative next-generation power sources for a wide range of applications due to the unique advantages, such as low self-discharge rate, high energy density, no memory effect and long cycle life [1–4]. However, it should be pointed out that the electrochemical performance of LIBs is usually restricted by the intrinsic properties of electrodes.

In the past decade, compared to commercial graphite anodes, some representative anodic materials with high specific capacities such as Si, Ge and Sn have attracted much attention [5–7]. However, these materials suffer from a huge volume change during lithiation/de-lithiation process. This severe volume variation will lead to the pulverization of the electrode and unstability of the formed SEI film, thus will impede the cycle stability [8,9]. Recently, transition metal oxides (TMOs) have been in the spotlight of research effort because of their high considerable capacity, abundant resource, as well as low cost [10–12]. Among them, Titanium oxide (TiO_2) is considered as a promising candidate for alternative electrode material owing to the advantages in terms of safety, low-cost, and environmental friendly [13,14]. For example, Yu et al. [15] developed a feasible templating method to fabricate porous rutile TiO_2 submicroboxes. On account of the porous thin shells, exceptionally high surface area, and embedded small primary nanoparticles, the obtained TiO_2 submicroboxes exhibit significantly improved lithium storage properties with negligible capacity degradation for more than 500 cycles. However, it is undeniable that pure TiO_2 anodes still experience low specific capacity [16] (~335 mA h g^{-1}) and poor rate performance. Therefore, it is still desirable to improve the

Conflict of Interest: The authors declare that they have no known competing financial interests or personal relationships that could have appeared to influence the work reported in this paper.

* Corresponding authors at: Key Laboratory of Mesoscopic Chemistry of MOE, State Key Laboratory of Coordination Chemistry, and Department of Chemistry and Chemical Engineering, Nanjing University, Nanjing 210023, PR China (Z. Jin); School of Chemistry and Chemical Engineering, Yancheng Institute of Technology, Yancheng 224051, PR China (Z. Jin, R. Jiang and J. Wu).

E-mail addresses: sunlin@nju.edu.cn (L. Sun), zhongjin@nju.edu.cn (Z. Jin).

https://doi.org/10.1016/j.flatc.2020.100152
Received 3 December 2019; Received in revised form 5 January 2020; Accepted 6 January 2020
Available online 08 January 2020

electrochemical performance of TiO_2-based electrodes.

It is first reported in 2011 that black titania oxide (TiO_{2-x}) has been produced after reducing white TiO_2 using hydrogen at 200 °C under 20 bar pressure for 5 days [17]. TiO_{2-x} exhibits high photocatalytic activity under solar light irradiation and improved lithium storage capability due to the abundant oxygen vacancy-contained characteristics [18–21]. Because of the presence of oxygen vacancies, TiO_{2-x} shows better electrical conductivity and higher lithium storage capacity than that of white TiO_2, which were also have been confirmed by our previous study [22]. However, for practical applications, such as electrical vehicles, the rate performance of TiO_{2-x} anodes are still not unsatisfactory and urgent to be enhanced. Recently, among the abundant two-dimensional materials, a new family of 2D materials called "MXene", comprising few atoms thick layers of transition metal carbides, nitrides, or carbonitrides, endow great promise in many applications [23]. Usually, MXene features with consummate conjunction of graphene oxide and graphene characters when compared with graphene [24,25]. MXene also possesses attractive advantages such as excellent mechanical flexibility and rapid lithium transport, which make them ideal 2D candidates for energy storage [26,27].

In this work, based on our previous research, we further report facile synthesis of 2D TiO_{2-x} nanoplate-decorated Ti_3C_2 MXene by solution method at room temperature. Herein, Ti_3C_2 MXene sheets act as excellent conductive two-dimensional support to load the black TiO_{2-x} nanoplate. At this point, the MXene carrier not only enables rapid reversible lithium ions and electrons transport at the interface, but also prevent the TiO_{2-x} aggregation during lithium ion insertion and extraction. On the other hand, the interposed TiO_{2-x} nanoplates also be served as the spacer to hold back MXene nanosheets restacking, thus preserving the active areas from being lost. When served as anodes in LIBs, the obtained TiO_{2-x}/Ti_3C_2 nanohybrids exhibit unprecedented rate performance and cycle stability. The specific capacity of TiO_{2-x}/Ti_3C_2 nanohybrids anode reaches as high as 135 mA h g^{-1} even cycled at high current density of 5 A g^{-1} (17 C) for 500 times. Even the charging-discharging process is performed at current density of 10 A g^{-1} (34 C), the specific capacity can still be maintained at around 110 mA h g^{-1}. This work is desirable expected to cater for a solution to foster the applications of TiO_{2-x} based anodes with ultra-high rate performance.

2. Experimental

2.1. Materials

Ti_3AlC_2 was purchased from Forsman Scientific (Beijing) Co., Ltd, China. Other chemicals and reagents were of analytical purity and used without further purification. Distilled water was used throughout.

2.2. Sample synthesis

2.2.1. Preparation of 2D TiO_{2-x} ($0 < x < 2$) nanoplate

According to our previous work [22], in a typical synthesis, adding dropwise 6 ml of hydrofluoric acid (HF) into a flask containing 50 ml of titanium butoxide (TBOT) under stirring. Then, the mixture was poured into a Teflon-line stainless steel autoclave, the autoclave was whereafter placed in a drying oven and kept at 190 °C for 24 h. After cooling, the formed jelly-like white precipitates were collected via centrifugation, washed and dried for further usage. In attempt to obtain black TiO_{2-x} nanoplate, a facile reduction process was carried out. Namely, 0.6 g of TiO_2 nanoplate and 0.6 g of sodium borohydride ($NaBH_4$) were grinded and mixed. Next, the mixture was loaded in a tube furnace with horizontal placement and annealing at 400 °C for 1 h under flowing nitrogen. The formed black product was washed with 1 M HCl solution and distilled water. Finally, black TiO_{2-x} nanoplate could be obtained after vacuum drying.

2.2.2. Preparation of Ti_3C_2 MXene nanosheets

For obtaining Ti_3C_2 MXene nanosheets, typically, 5 g of Ti_3AlC_2 was added to 50 ml of 40% HF solution and stirred at room temperature for three days, then centrifuged, washed several times with deionized water, and dried under vacuum at 60 °C overnight.

2.2.3. Synthesis of TiO_{2-x}/Ti_3C_2 nanohybrids

In a typical synthesis, 0.4 g of Ti_3C_2 nanosheets were added to 20 ml DMSO and stirred at room temperature for 18 h, then centrifuged, washed several times with deionized water. After that, Ti_3C_2 were dispersed into 200 ml of deionized water under nitrogen atmosphere, and ultrasonic dispersion for 1 h. On the other hand, 0.4 g of TiO_{2-x} were dispersed into 50 ml of deionized water and ultrasonic dispersion for 20 min. Finally, mixing the dispersed Ti_3C_2 solution and TiO_{2-x} dispersion and further stirred at inert atmosphere overnight. After that, the products were filtered and washed several times with deionized water, and dried under vacuum at 50 °C overnight.

2.3. Materials characterization

Powder X-ray diffraction (PXRD) data were collected on a Bruker D8 Advance instrument using a Cu Kα radiation (λ = 1.54056 Å) at room temperature. EPR analysis was conducted on Bruker EMX-10/12 apparatus. SEM images and Energy Dispersive Spectroscopy (EDS) were obtained on a Nova NanoSEM 450 field-emission scanning electron microscope at an acceleration voltage of 10 kV and 20 kV, respectively. Transmission electron microscopy (TEM) characterization was carried out using a JEM-2100F (Japan). Atomic force microscopy (AFM) was performed using a Si CANTILEVER with contact mode. X-ray photoelectron spectroscopy (XPS) measurements were recorded with a ESCALAB 250Xi. Nitrogen sorption isotherms were collected at 77 K (Micrometrics ASAP 2020 analyzer) after vacuum degassing of the sample at 120 °C for 10 h.

2.4. Electrochemical measurements

CR2025 cells were utilized as standard battery pack and assembled in an argon-filled glove box to evaluate electrochemical properties. TiO_{2-x}/Ti_3C_2 electrode was constructed with active material, conductive graphite, and polyvinylidene fluoride (PVDF) binder, the mass ratio was 8:1:1. Firstly, the three components were mixed and stirred in N-Methyl pyrrolidone (NMP) solvent and blade-coated on a piece of Cu foil. The foil was cut into disks of 14 mm in diameter after vacuum drying at 110 °C overnight. The electrolyte consisted of a solution of 1 M $LiPF_6$ in a mixture of 1:1 (vol/vol) dimethyl carbonate (DMC)/ethylene (EC) (Shenzhen Kejingstar Technology Ltd., China). The counter electrodes were pure Li foils. The battery measurements were performed on a Neware battery testing device (Shenzhen, China) at the constant current mode over the range of 0.01–3 V. Cyclic voltammetry (CV) curves were obtained with voltage window ranging from 0.01 to 3 V using a CHI600D electrochemical workstation (Chenhua, Shanghai, China). The specific capacities were calculated based on the total weight of TiO_{2-x}/Ti_3C_2 hybrids. The theoretical capacity of TiO_{2-x} and Ti_3C_2 was considered as 335 and 320 mA h g^{-1}, respectively. For each electrode, the loading amount of active materials is around 1 mg cm^{-2}.

3. Results and discussions

The schematic for the preparation of 2D TiO_{2-x}/Ti_3C_2 nanohybrids is depicted in Scheme 1. Briefly, Ti_3C_2 MXene is fabricated by goal-oriented etching Al layers of the precursor (MAX, Ti_3AlC_2) using HF and finally delaminates into few or multi-layered MXene sheets. Subsequently, PXRD patterns SEM images of 2D black TiO_{2-x} nanoplate and the white TiO_2 precursors were shown in Fig. 1. Fig. 1a shows the PXRD patterns of white TiO_2 and black TiO_{2-x}, respectively. It is revealed that the black TiO_{2-x} still basically maintain the anatase phase structure after

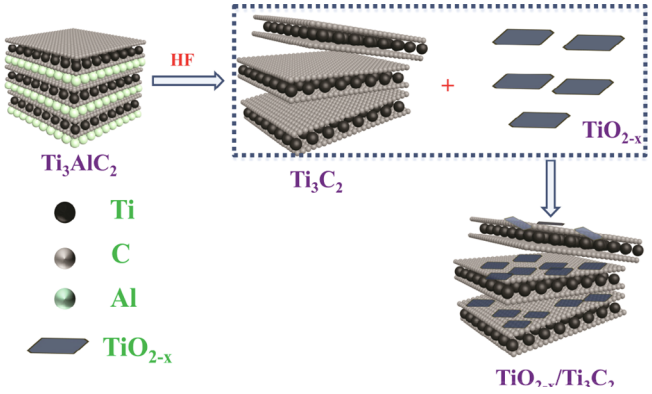

Scheme 1. Schematic of the formation of TiO_{2-x}/Ti_3C_2 nanohybrids.

$NaBH_4$ reduction, and the morphology was still unchanged, as shown in Fig. 1b and c. Moreover, the further AFM characterization shows that the thickness of black TiO_{2-x} nanoplate was nearly 3 nm were decorated on the surface and the interspaces of Ti_3C_2 MXene to form TiO_{2-x}/Ti_3C_2 nanohybrids under ambient conditions.

XRD analysis associated with Ti_3AlC_2, Ti_3C_2, and TiO_{2-x}/Ti_3C_2 were carried out to investigate the crystallographic phase of the products, which are shown in Fig. 2a. After HF treatment, the most intense XRD peak of Ti_3AlC_2 ($2\theta \approx 38^\circ$, black curve in Fig. 2a) disappears. The (0 0 2) peak of Ti_3AlC_2 at 9.5° is shifted to lower 8.8° and is broadened in both Ti_3C_2 (red curve) and TiO_{2-x}/Ti_3C_2 nanohybrids (blue curve), implying the interlayer spacings were substantial expanded, as well as meaning that Al layers have been successfully removed of by etching and formation of Ti_3C_2 MXene. In addition, it is worth considering that species like atoms or molecules with unpaired electrons play an important role in some applications, which can qualitatively and quantitatively measured by EPR. In this regard, EPR measurements were carried out under ambient condition at 110 K to verify the presence oxygen vacancies. As shown in Fig. 2b, the pink line for the white TiO_2 nanoplate shows a negligible signal peak, while the black TiO_{2-x} nanoplate exhibits a very strong EPR signal centered on the magnetic field strength of 3478 G, which can be attributed to the unpaired electrons trapped on the surface oxygen vacancies [28,29].

The general morphology and microstructures of the Ti_3C_2 and TiO_{2-x}/Ti_3C_2 hybrids were characterized by SEM, TEM and HRTEM. Fig. 3a and d show the SEM images of Ti_3C_2 and TiO_{2-x}/Ti_3C_2, respectively. It can be clearly seen from Fig. 3a that the interlayers of bulk Ti_3AlC_2 material (Fig. 4a) are propped open after HF treatment, and the surface

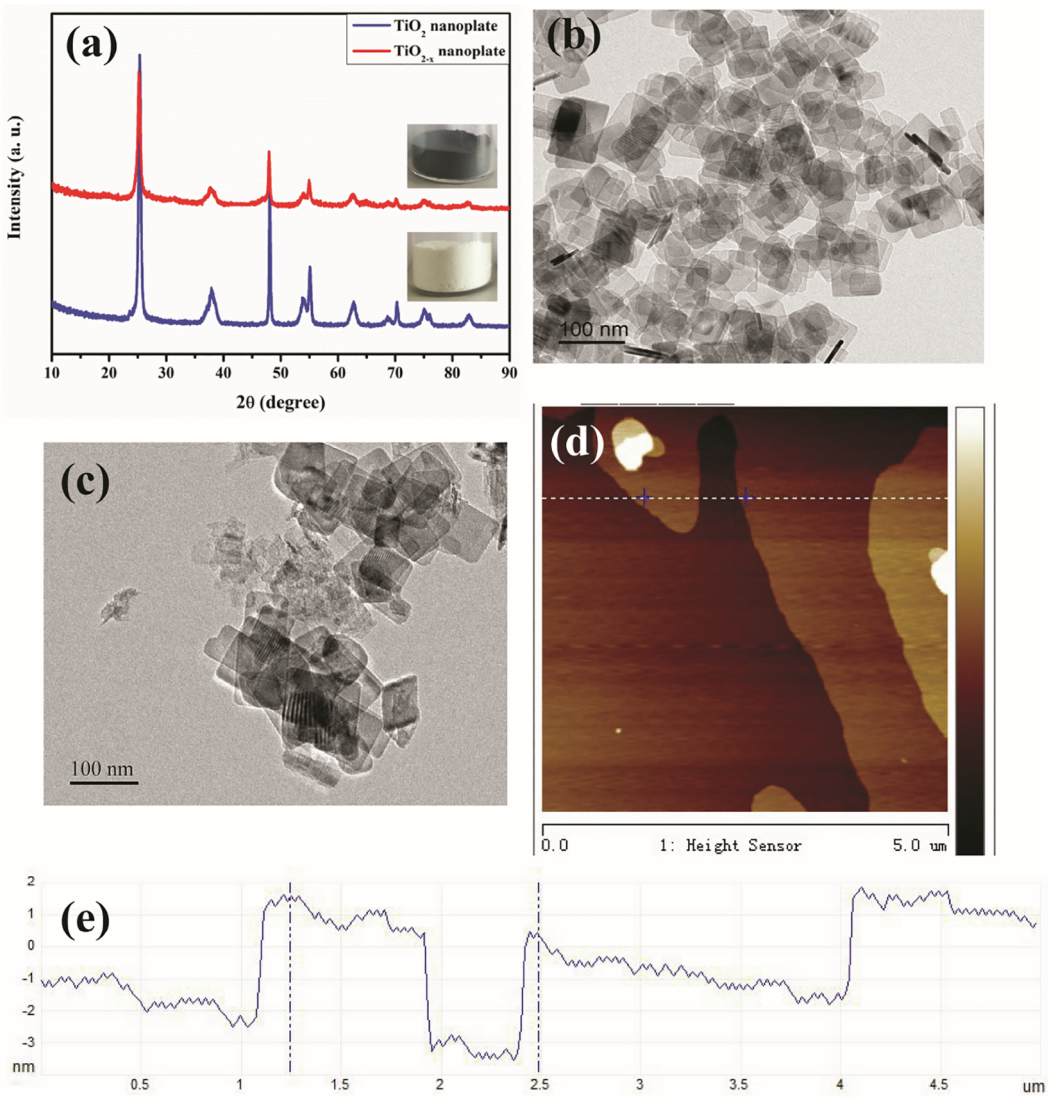

Fig. 1. (a) PXRD patterns of white TiO_2 and black TiO_{2-x} nanoplates; SEM images of TiO_2 nanoplate (b) and TiO_{2-x} nanoplate (c); (d) Contact mode AFM image of TiO_{2-x} nanoplate and (e) the line profiles taken along the white line in image d.

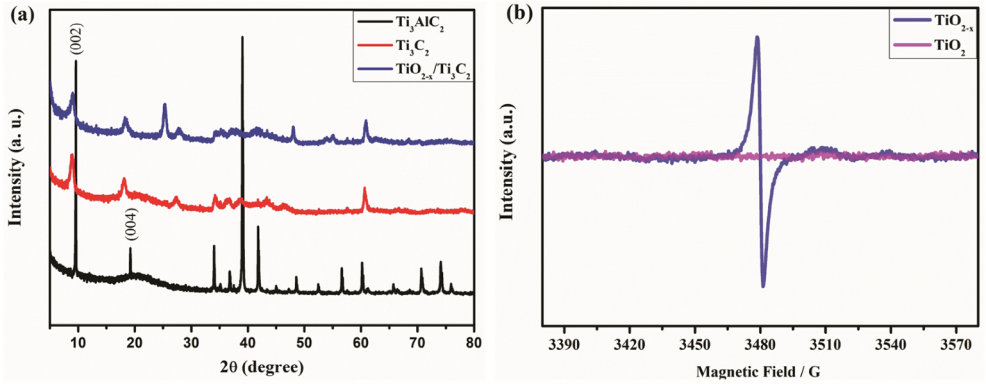

Fig. 2. (a) PXRD patterns of Ti_3AlC_2 (black), Ti_3C_2 (red), and TiO_{2-x} /Ti_3C_2 (blue); (b) EPR spectrums of white TiO_2 and black TiO_{2-x}.

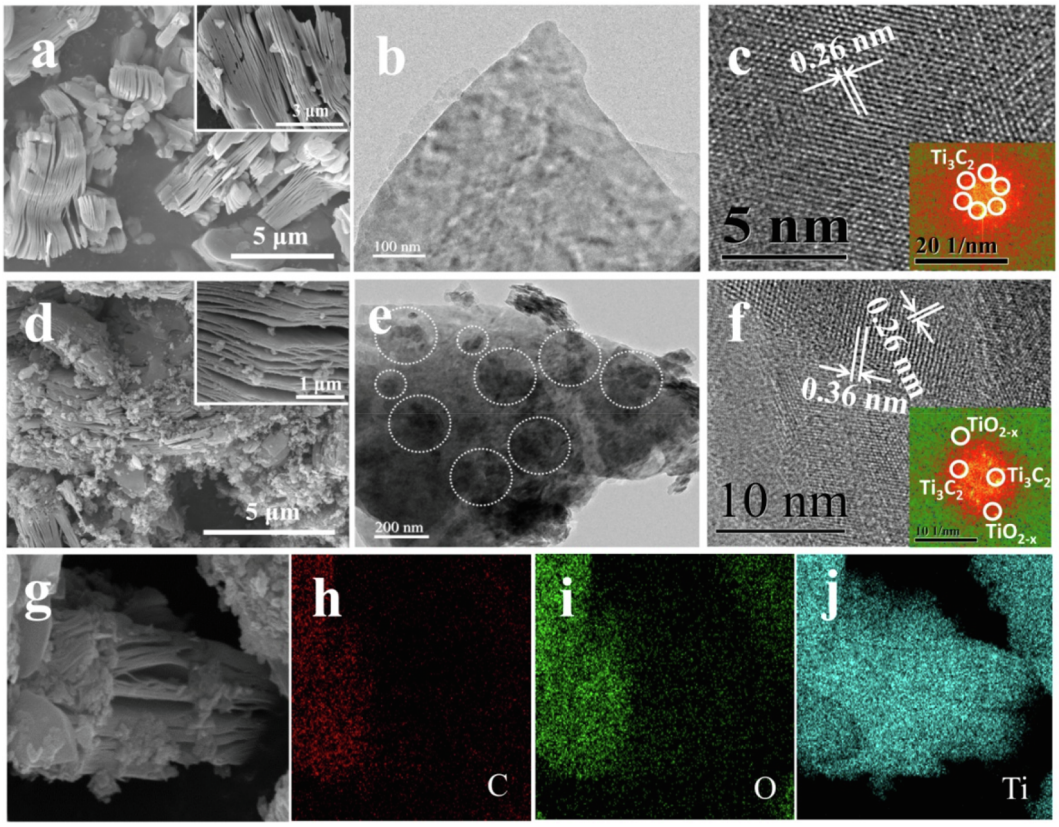

Fig. 3. (a, d) SEM images of Ti_3C_2 and TiO_{2-x}/Ti_3C_2 nanohybrids, insert images in Fig. 3a and d show the corresponding magnified image, respectively; (b, e) TEM images of Ti_3C_2 and TiO_{2-x}/Ti_3C_2 nanohybrids; (c, f) HRTEM images of Ti_3C_2 and TiO_{2-x}/Ti_3C_2 composite; (g-j) EELS maps of (h) C, (i) O, and (j) Ti elements.

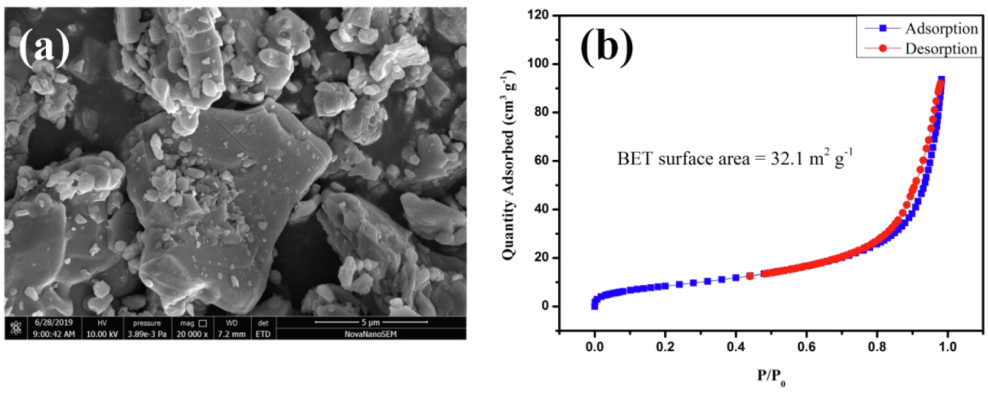

Fig. 4. (a) SEM image of Ti_3AlC_2 and (b) Typical nitrogen adsorption isotherms of TiO_{2-x}/Ti_3C_2 nanohybrids.

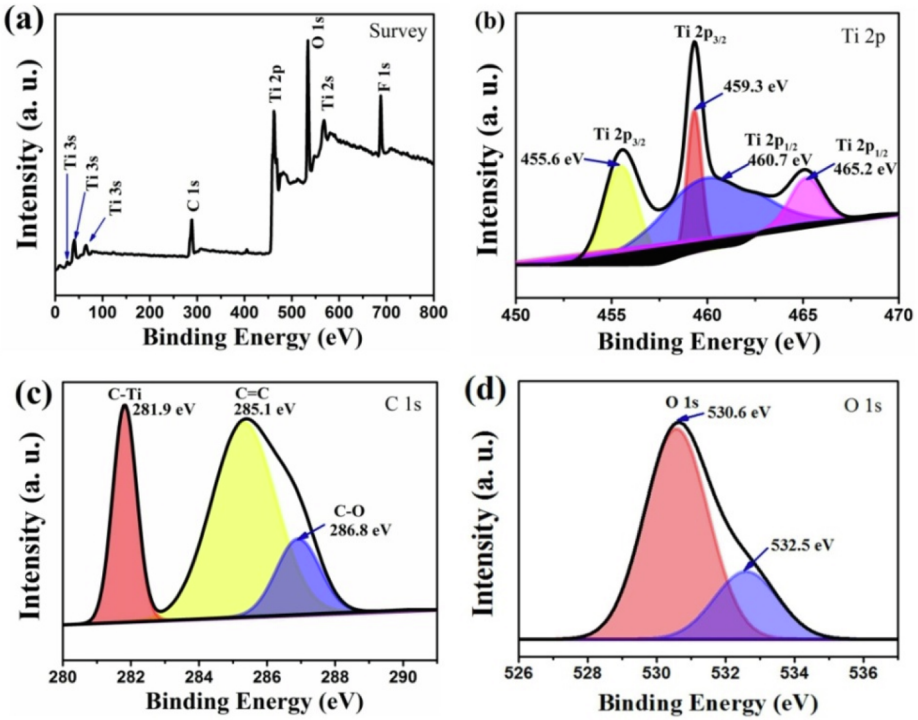

Fig. 5. XPS spectra of (a) fully scanned spectra, (b) Ti 2p, (c) C 1s, and (d) O 1s in TiO_{2-x}/Ti_3C_2 hybrids.

of the obtained Ti_3C_2 is smooth, which can also be confirmed by TEM (Fig. 3b). After formation of TiO_{2-x}/Ti_3C_2 nanohybrids, as shown in Fig. 3d and e, the TiO_{2-x} nanoplates are distributed on the surface and interspaces of Ti_3C_2 multilayers (the circle location in Fig. 3e). Moreover, Fig. 3c and f exhibit the HRTEM images of Ti_3C_2 and TiO_{2-x}/Ti_3C_2, further confirming the production of pure Ti_3C_2 and TiO_{2-x}/Ti_3C_2 nanohybrids. The clear lattice fringes with fringes spacing of 0.26 nm and 0.36 nm can be indexed as the Ti_3C_2 and anatase TiO_{2-x}, respectively. The insert fast-fourier transform (FFT) patterns in Fig. 3c and f also confirm the successful preparation of Ti_3C_2 and TiO_{2-x}/Ti_3C_2 nanohybrids. Fig. 3g-j show the corresponding element mapping images of the TiO_{2-x}/Ti_3C_2 nanohybrids, the relatively less amount C and O elements (Fig. 3h and i) are mainly attributed to the uneven distribution of TiO_{2-x} within Ti_3C_2 multilayered nanosheets. At the same time, it should be noted that after intercalation, the TiO_{2-x}/Ti_3C_2 nanohybrids get high specific surface area of 32.1 $m^2\ g^{-1}$, as shown in Fig. 4b.

The chemical composition and chemical states of Ti, C and O elements in TiO_{2-x}/Ti_3C_2 nanohybrids were investigated using X-ray photoelectron spectroscopy (XPS) technique. Fig. 5a illustrates the survey scan of the TiO_{2-x}/Ti_3C_2 hybrids, the chemical compositions of Ti, C, O and F were detected. Among them, the only impurity F element can be attributed to the residue F ions from the HF solution [30]. In the Ti 2p XPS spectra, as shown in Fig. 5b, the Ti 2p XPS spectra of TiO_{2-x}/Ti_3C_2 hybrids can be deconvoluted into four peaks. The two peaks located at binding energies of 459.3 eV (Ti $2p_{3/2}$) and 465.2 eV (Ti $2p_{1/2}$) are attributed to the lattice Ti-O bond in TiO_{2-x} [31]. While the other two peaks at binding energies of 455.6 eV (Ti $2p_{3/2}$) and 460.7 eV (Ti $2p_{1/2}$) correspond to the lattice of Ti-C bond [32,33]. Furthermore, for C 1s XPS spectrum, three peaks at 281.9 eV, 285.1 eV and 286.8 eV can be observed in Fig. 5c after peak fitting, which can be assigned to the C-Ti, C=C and C-O, respectively [34]. Besides, the O 1s XPS spectrum (Fig. 5d) can be split into two peaks centered at 530.6 eV and 532.5 eV which belong to Ti-O-Ti and Ti-O-H bonds, respectively [35].

The electrochemical performances of TiO_{2-x}/Ti_3C_2 anodic LIBs were investigated by using a 2025 type coin cell assembly with pure lithium foil as the counter electrode. Fig. 6a shows the cyclic voltammetry (CV) test results of TiO_{2-x}/Ti_3C_2 nano-hybrid electrode for first three cycles with a voltage window of 0–3 V at a scan rate of 0.2 mV s^{-1} vs. Li/Li^+. During the first lithiation step, two evident oxidation peaks which located at 1.72 and 0.63 V, as well as a weak broad peak at 2.37 V can also be detected, which can be assigned to the lithiation of TiO_{2-x} and Ti_3C_2, respectively [36]. It should be considered that, in the subsequent cycles, the peaks at 1.72 and 0.63 V are disappeared, which is mainly ascribed to the formation of solid electrolyte interphase (SEI) film and the trapped Li^+ within the MXene layers [37]. It is a remarkable fact that there is slight shift and decrement regarding these peaks, implying a two-phase reaction mechanism during lithiation and de-lithiation processes based on the following equations [25].

$$Ti_3C_2 + xLi^+ + 4e^- \leftrightarrow Ti_3C_2Li_x \quad (1)$$

$$TiO_{2-x} + xLi^+ + xe^- \leftrightarrow Li_xTiO_{2-x} \quad (2)$$

Moreover, during the anodic process, reductive peaks at 1.07 and 2.55, as well as 2.05 V can be attributed to the de-lithiation of TiO_{2-x} and TiO_{2-x}/Ti_3C_2 nano-hybrids. Consider that after the first scan, the reductive peaks at 1.07 and 2.05 V remain nearly unchanged in terms of the intensity and position, proving the stability and fairly high electrochemical activity of TiO_{2-x}/Ti_3C_2 nano-hybrid electrode. Fig. 6b exhibits the typical first three cycle discharge-charge voltage profiles of the TiO_{2-x}/Ti_3C_2 electrode. The first discharge and charge specific capacities of TiO_{2-x}/Ti_3C_2 electrode are 287 and 176 mA h g^{-1}, respectively, resulting in a corresponding coulombic efficiency of 61.3%. However, in the next two cycles, the coulombic efficiency goes up to more than 90%. The resulting low first cycle coulombic efficiency was mainly ascribed to the formation of SEI film and the irreversible reactions between the electrode and the electrolyte. At the same time, the apparent voltage plateaus between in 1.5–2 V in both charge and discharge curves are attributed to the de-lithiation and lithiation of TiO_{2-x}/Ti_3C_2 hybrids, the phenomenon is completely consistent with the result of CV examination.

The rate capability of TiO_{2-x}/Ti_3C_2 was further explored at increasing current densities, the test results were illustrated in Fig. 6c. The electrode afforded specific capacities of 206, 187, 168, 152, 131, and 115 mA h g^{-1} at current densities of 0.1, 0.5, 1, 2, 5, and 10 A g^{-1},

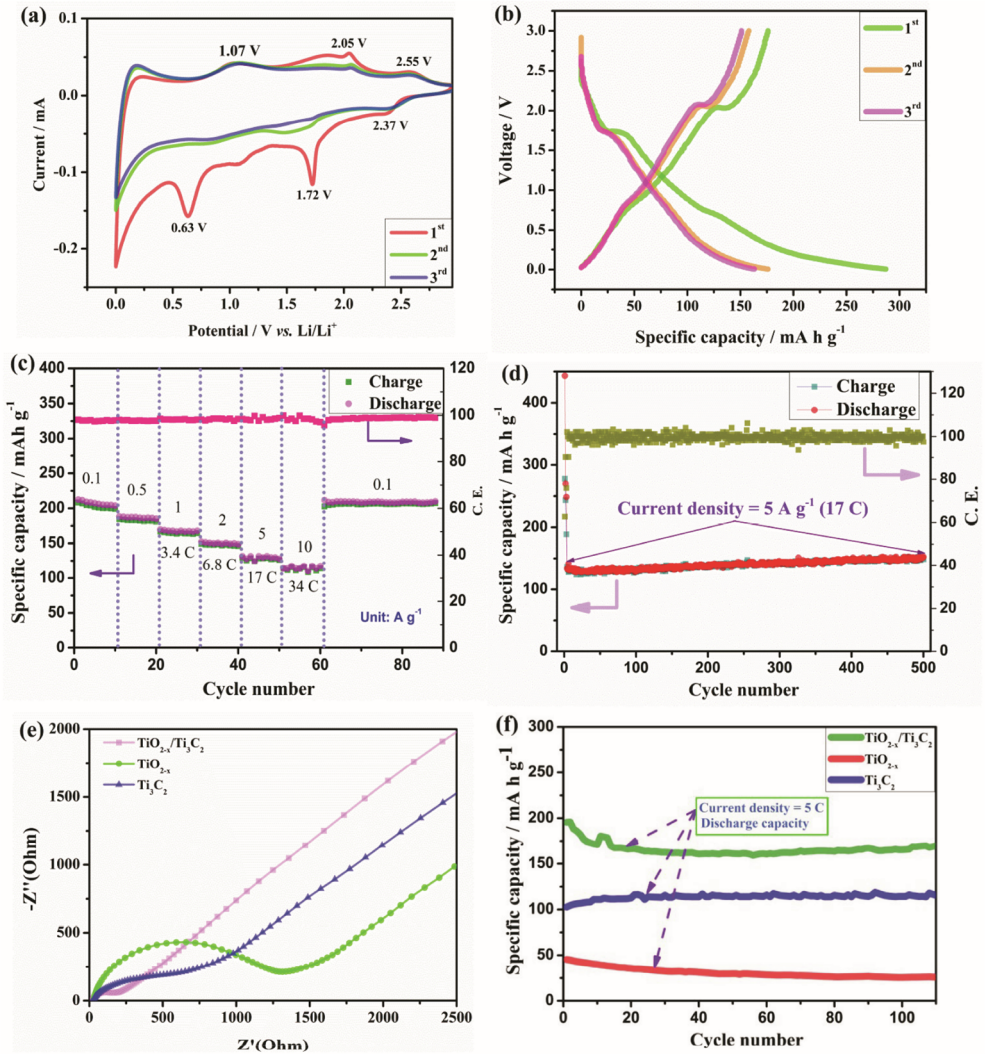

Fig. 6. (a) Cyclic voltammetry (CV) curve of TiO_{2-x}/Ti_3C_2 hybrid electrode; (b) Voltage profiles of the TiO_{2-x}/Ti_3C_2 hybrid electrode; (c) Rate performance of TiO_{2-x}/Ti_3C_2 electrode cycled at different current densities; (d) Long-term cycling stability of the TiO_{2-x}/Ti_3C_2 electrode; (d) EIS profiles of pristine Ti_3C_2, TiO_{2-x} and TiO_{2-x}/Ti_3C_2, respectively and (e) The cycling stability comparison of TiO_{2-x}, Ti_3C_2 and TiO_{2-x}/Ti_3C_2 hybrid electrode when cycling at the same current density.

respectively. The electrode showed excellent reversibility with the specific discharge capacity recovered to the starting value when the current density returned to 0.1 A g^{-1} after cycling at high current densities. It is worth considering that based on the materials' theoretical specific capacities and the actual active material loading amount on the electrode, the current density of 10 A g^{-1} corresponds to 34 C. Thus, even working at high current density of 34 C, the electrode still maintains a high specific capacity of 115 mA h g^{-1}, which surpassing most of the reported works, as shown in Table 1. For comparison, we also fabricate bare TiO_{2-x} anodic LIBs. It can be clearly seen from Fig. 6f that, when cycling at the same current density of 5 C, the bare TiO_{2-x} electrode exhibits sharply decreased capacity retention of merely 25 mA h g^{-1}. However, TiO_{2-x}/Ti_3C_2 electrode still delivers a high specific capacity of around 170 mA h g^{-1}. On the other hand, thus strongly demonstrating that after incorporation with Ti_3C_2, the electrical conductivity of TiO_{2-x}/Ti_3C_2 electrode has been significantly improved, which in-turn enhancing the rate performance.

The long-term cycling stability of the TiO_{2-x}/Ti_3C_2 electrode was evaluated by cycling at a large current density of 5 A g^{-1} (17 C). Before the lone-term cycling, the electrode was firstly activated at a small current density. From Fig. 6d, it can be seen that in the initial cycles, the specific capacity of the TiO_{2-x}/Ti_3C_2 electrode was sharply decreased due to the electrode activation process. After the electrode goes stability, the electrode exhibits a significantly stable specific capacity of around 130 mA g^{-1} even working at high current density of 5 A g^{-1} (17 C) for 500 cycles.

Moreover, electrochemical impedance spectroscopy (EIS) was performed to further verify that the TiO_{2-x}/Ti_3C_2 nano-hybrid perform well in LIBs. The EIS spectrums of Ti_3C_2, TiO_{2-x} and TiO_{2-x}/Ti_3C_2 electrodes are shown in Fig. 6e. It is clearly seen from Fig. 6e that a semicircle in high-frequency region is formed and in the low-frequency region the spectra is linear. It is well known that during the discharge process, in some instances, both of the charge transfer reaction between the electrodes and the formed SEI film lead to the semicircle in the high-frequency region. Besides, the linear behavior in the low-frequency region is ascribed to the diffusion of Li ions on the electrodes [62,63]. From Fig. 6d, it is clearly shown that TiO_{2-x}/Ti_3C_2 electrode shows a much smaller semicircular diameter among three electrodes, implying the best charge transfer efficiency. The result was ascribed to the better conductivity of TiO_{2-x}/Ti_3C_2 which possibly related to the formation of heterojunctions between TiO_{2-x} and Ti_3C_2 after hybridization [64], and this corresponded to the excellent rate performance of TiO_{2-x}/Ti_3C_2 electrode.

Table 1
Electrochemical properties of various Ti-based anodic electrodes.

Anode	The mass loading levels	Rate Performance	Cycle Performance	Ref
TiO_2@C	0.8–1.0 mg cm^{-2}	127 mA h g^{-1}/20C 159 mA h g^{-1}/10C 177 mA h g^{-1}/5C 195 mA h g^{-1}/1C	133 mA h g^{-1}(3000th)/10C	[38]
N-TiO_2@C	None	204.1 mA h g^{-1}/10C 221.6 mA h g^{-1}/5C 236.9 mA h g^{-1}/2C 311.5 mA h g^{-1}/1C	235.8 mA h g^{-1}(250th)/1C	[39]
TiO_2	2 mg cm^{-2}	60 mA h g^{-1}/5A g^{-1} 80 mA h g^{-1}/3A g^{-1} 105 mA h g^{-1}/1.5A g^{-1} 140 mA h g^{-1}/0.5A g^{-1} 164 mA h g^{-1}/0.3A g^{-1}	103 mA h g^{-1}(1000th)/1.5A g^{-1}	[40]
TiO_2	2.78 mg cm^{-2}	160 mAh g^{-1}/5C 178 mAh g^{-1}/2.5C 199 mAh g^{-1}/1C 220 mAh g^{-1}/0.5C	197 mAh g^{-1}(1000th)/1C	[41]
Nb-TiO_2	2 mg cm^{-2}	137.1 mA h g^{-1}/2C 190.7 mA h g^{-1}/1C 244 mA h g^{-1}/0.5C 386.8 mA h g^{-1}/0.2C	246.8 mA h g^{-1}(100th)/0.2C	[42]
TiO_2-MCs@CC	4 mg cm^{-2}	75 mA h g^{-1}/4A g^{-1} 110 mA h g^{-1}/2A g^{-1} 140 mA h g^{-1}/1A g^{-1} 160 mA h g^{-1}/0.5A g^{-1} 175 mA h g^{-1}/0.2A g^{-1}	73.7 mA h g^{-1}(1000th)/2A g^{-1}	[43]
PVP@TNT	None	50 mA h g^{-1}/5C 70 mA h g^{-1}/3C 90 mA h g^{-1}/2C 100 mA h g^{-1}/1C	140 mA h g^{-1}(100th)/0.2C	[44]
$Li_4Ti_5O_{12}$@TiO_2	None	113.7 mA h g^{-1}/10C 122.9 mA h g^{-1}/5C 145.4 mA h g^{-1}/1C	177.3 mA h g^{-1}(660th)/0.5C	[45]
B-TNAs@PANI	None	88 mA h g^{-1}/200C 113 mA h g^{-1}/20C	86%(2000th)/1C	[46]
C-TiO_2@G	0.8 mg cm^{-2}	220 mA h g^{-1}/4.5A g^{-1}	338.6 mA h g^{-1}(200th)/1.5A g^{-1}	[47]
TiO_2@rGO	1.49 mg cm^{-2}	85.6 mA h g^{-1}/10C 136.6 mA h g^{-1}/2C	158 mA h g^{-1}(3000th)/10C	[48]
M-TiO_2-GS	2 mg cm^{-2}	76 mA h g^{-1}/20C 108 mA h g^{-1}/10C	94 mA h g^{-1}(3500th)/5C	[49]
CNTs–C@TiO_2	2.5 mg cm^{-2}	72 mA h g^{-1}/1.6A g^{-1}	205.5 mA h g^{-1}(200th)/0.1A g^{-1}	[50]
NCS@$TiO_{2-\delta}$@RGO	1–1.5 mg cm^{-2}	120 mA h g^{-1}/10C	300 mA h g^{-1}(400th)/5C	[51]
HNW-TMS	0.5–0.8 mg cm^{-2}	173.8 mA h g^{-1}/1A g^{-1}	141.1 mA h g^{-1}(200th)/1A g^{-1}	[52]
C/N-TiO_2	1.5–2.0 mg cm^{-2}	160.5 mA h g^{-1}/1A g^{-1}	268.2 mA h g^{-1}(600th)/0.1A g^{-1}	[53]
TLC-TOC	1.5–2.6 mg cm^{-2}	85 mA h g^{-1}/6.4A g^{-1}	150 mA h g^{-1}(10000th)/3A g^{-1}	[54]
TiO_2	0.77 mg cm^{-2}	51.3 mA h g^{-1}/20C	120.5 mA h g^{-1}(1000th)/1C	[55]
TiO_2@Fe_2O_3	1–2 each electrode	120 mA h g^{-1}/1A g^{-1}	571 mA h g^{-1}(150th)/0.1A g^{-1}	[56]
Ti_3C_2	None	114.5 mA h g^{-1}/2A g^{-1}	329.5 mA h g^{-1}(590th)/0.1A g^{-1}	[57]
HHM-TiO_2@C	None	126 mA h g^{-1}/20C	200 mA h g^{-1}(500th)/1C	[58]
TiO_2@MXene	1.0–1.1 mg cm^{-2}	140 mA h g^{-1}/2A g^{-1}	167 mA h g^{-1}(200th)/0.5A g^{-1}	[25]
SnO_x@Ti_3C_2	None	190 mA h g^{-1}/2A g^{-1}	450 mA h g^{-1}(250th)/0.2A g^{-1}	[59]
Si@Ti_3C_2 MXene	0.5–0.8 mg cm^{-2}	80 mA h g^{-1}/3A g^{-1}	188 mA h g^{-1}(150th)/0.2A g^{-1}	[60]
S-Ti_3C_2	0.4–0.8 mg cm^{-2}	136.6 mA h g^{-1}/5A g^{-1}	135 mA h g^{-1}(1000th)/2A g^{-1}	[61]
MoS_2@Ti_3C_2	0.29 mg cm^{-2}	131.6 mA h g^{-1}/1A g^{-1}	131.6 mA h g^{-1}(280th)/1A g^{-1}	[62]
TiO_{2-x}/Ti_3C_2	~1 mg cm^{-2}	**115 mA h g^{-1}/34C**	**131 mA h g^{-1}(500th)/17C**	**this work**

4. Conclusions

In conclusion, the nano-hybrids of 2D TiO_{2-x} nanoplate-decorated multi-layered Ti_3C_2 MXene are prepared by a step-by-step assembly solution method. The synergistic effect of the presence of Ti_3C_2 MXene and TiO_{2-x} nanoplates are beneficial for the hybrid material fabrication and the improved battery performance. This novel material design efficiently combines the high electrical conductivity of Ti_3C_2 MXene and improved capacity of oxygen vacancy-contained TiO_{2-x} nanoplates. As a result, the TiO_{2-x}/Ti_3C_2 hybrid anodes exhibit excellent cyclability and rate capability, which may offer a new concept for developing ultra-stable and fast anodes for next-generation LIBs.

CRediT authorship contribution statement

Lin Sun: Conceptualization, Writing - original draft. **Jie Xie:** Data curation, Investigation. **Lei Zhang:** Software. **Ruiyu Jiang:** Funding acquisition. **Jun Wu:** Writing - review & editing. **Lele Fan:** Software. **Rong Shao:** Resources. **Zhidong Chen:** Resources. **Zhong Jin:** Supervision.

Acknowledgements

This work was supported by the Research Fund of the Natural Science Foundation of Jiangsu Province (no. BK20181056), Jiangsu Province Cultivation base for State Key Laboratory of Photovoltaic Science and Technology (SKLPST201901), the Natural Science Foundation of Jiangsu Province-General Program (BK20171273),

Natural Science Foundation of the Jiangsu Higher Education Institutions of China (19KJA540001), “Six Talent Peak” High-level Talent Project (JNHB-068).

References

[1] D. Gu, W. Li, F. Wang, H. Bongard, B. Spliethoff, W. Schmidt, C. Weidenthaler, Y. Xia, D. Zhao, F. Schüth, Angew. Chem. Int. Ed. 54 (2015) 7060–7064.
[2] D. Larcher, J.M. Tarascon, Nat. Chem. 7 (2014) 19.
[3] A. Manthiram, X. Yu, S. Wang, Nat. Rev. Mater. 2 (2017) 16103.
[4] Y. Zhao, X. Li, B. Yan, D. Xiong, D. Li, S. Lawes, X. Sun, Adv. Energy Mater. 6 (2016) 1502175.
[5] L. Sun, F. Wang, T. Su, H. Du, ACS Appl. Mater. Interfaces 9 (2017) 40386–40393.
[6] J. Liu, X. Lin, X. Chen, Z. Shen, M. Chi, J. Niu, H. Zhang, J. Huang, J. Li, Chem. Commun. 53 (2017) 13125–13128.
[7] W. Xiao, J. Zhou, L. Yu, D. Wang, X.W. Lou, Angew. Chem. Int. Ed. 55 (2016) 7427–7431.
[8] Y. Shi, J. Wan, J.-Y. Li, X.-C. Hu, S.-Y. Lang, Z.-Z. Shen, G. Li, H.-J. Yan, K.-C. Jiang, Y.-G. Guo, R. Wen, L.-J. Wan, Nano Energy 61 (2019) 304–310.
[9] W. Luo, Y. Wang, L. Wang, W. Jiang, S.-L. Chou, S.X. Dou, H.K. Liu, J. Yang, ACS Nano 10 (2016) 10524–10532.
[10] C. Wang, X.-D. Zhu, Y.-C. Mao, F. Wang, X.-T. Gao, S.-Y. Qiu, S.-R. Le, K.-N. Sun, Chem. Commun. 55 (2019) 1237–1240.
[11] T.S. Dörr, S. Fleischmann, M. Zeiger, I. Grobelsek, P.W. de Oliveira, V. Presser, Chem. Eur. J. 24 (2018) 6358–6363.
[12] Z.-W. Zhou, L. Pan, Y.-T. Liu, X.-D. Zhu, X.-M. Xie, Chem. Commun. 54 (2018) 4790–4793.
[13] M. Zou, Z. Ma, Q. Wang, Y. Yang, S. Wu, L. Yang, S. Hu, W. Xu, P. Han, R. Zou, A. Cao, J. Mater. Chem. A 4 (2016) 7398–7405.
[14] D. Wang, Z. Shan, R. Na, W. Huang, J. Tian, J. Power Sources 337 (2017) 11–17.
[15] X.-Y. Yu, H.B. Wu, L. Yu, F.-X. Ma, X.W. Lou, Angew. Chem. Int. Ed. 54 (2015) 4001–4004.
[16] D. Yan, Y. Bai, C. Yu, X. Li, W. Zhang, J. Alloys Compd. 609 (2014) 86–92.
[17] X. Chen, L. Liu, P.Y. Yu, S.S. Mao, Science 331 (2011) 746.
[18] T. Lin, C. Yang, Z. Wang, H. Yin, X. Lü, F. Huang, J. Lin, X. Xie, M. Jiang, Energy Environ. Sci. 7 (2014) 967–972.
[19] G. Panomsuwan, A. Watthanaphanit, T. Ishizaki, N. Saito, Phys. Chem. Chem. Phys. 17 (2015) 13794–13799.
[20] X. Feng, P. Wang, J. Hou, J. Qian, C. Wang, Y. Ao, Chem. Eng. J. 352 (2018) 947–956.
[21] Y. Yang, W. Shi, S. Liao, R. Zhang, S. Leng, J. Alloys Compd. 746 (2018) 619–625.
[22] L. Sun, J. Xie, Q. Li, F. Wang, X. Xi, L. Li, J. Wu, R. Shao, Z. Chen, J. Solid State Electrochem. 23 (2019) 803–810.
[23] S.B. Ambade, R.B. Ambade, W. Eom, S.H. Noh, S.H. Kim, T.H. Han, Adv. Mater. Interfaces 5 (2018) 1801361.
[24] Y. Tian, Y. An, J. Feng, ACS Appl. Mater. Interfaces 11 (2019) 10004–10011.
[25] Y.-T. Liu, P. Zhang, N. Sun, B. Anasori, Q.-Z. Zhu, H. Liu, Y. Gogotsi, B. Xu, Adv. Mater. 30 (2018) 1707334.
[26] M.R. Lukatskaya, O. Mashtalir, C.E. Ren, Y. Dall’Agnese, P. Rozier, P.L. Taberna, M. Naguib, P. Simon, M.W. Barsoum, Y. Gogotsi, Science 341 (2013) 1502.
[27] M. Ghidiu, M.R. Lukatskaya, M.-Q. Zhao, Y. Gogotsi, M.W. Barsoum, Nature 516 (2014) 78.
[28] L. Xu, L. Yang, E.M.J. Johansson, Y. Wang, P. Jin, Chem. Eng. J. 350 (2018) 1043–1055.
[29] F. Liu, N. Feng, L. Yang, Q. Wang, J. Xu, F. Deng, J. Phys. Chem. C 122 (2018) 10948–10955.
[30] Y. Li, Z. Yin, G. Ji, Z. Liang, Y. Xue, Y. Guo, J. Tian, X. Wang, H. Cui, Appl. Catal., B 246 (2019) 12–20.
[31] L. Zheng, S. Han, H. Liu, P. Yu, X. Fang, Small 12 (2016) 1527–1536.
[32] M. Rester, J. Neidhardt, P. Eklund, J. Emmerlich, H. Ljungcrantz, L. Hultman, C. Mitterer, Mater. Sci. Eng. 429 (2006) 90–95.
[33] C. Peng, P. Wei, X. Li, Y. Liu, Y. Cao, H. Wang, H. Yu, F. Peng, L. Zhang, B. Zhang, K. Lv, Nano Energy 53 (2018) 97–107.
[34] C. Liu, Q. Xu, Q. Zhang, Y. Zhu, M. Ji, Z. Tong, W. Hou, Y. Zhang, J. Xu, J. Mater. Sci. 54 (2019) 2458–2471.
[35] H. Huang, Y. Song, N. Li, D. Chen, Q. Xu, H. Li, J. He, J. Lu, Appl. Catal., B 251 (2019) 154–161.
[36] C. Yang, Y. Liu, X. Sun, Y. Zhang, L. Hou, Q. Zhang, C. Yuan, Electrochim. Acta 271 (2018) 165–172.
[37] D. Sun, M. Wang, Z. Li, G. Fan, L.-Z. Fan, A. Zhou, Electrochem. Commun. 47 (2014) 80–83.
[38] C. Zhang, S. Liu, Y. Qi, F. Cui, X. Yang, Chem. Eng. J. 351 (2018) 825–831.
[39] Y. Wang, Y. Lu, R. Luo, Y. Zhang, Y. Guo, Q. Yu, X. Liu, J.-K. Kim, Y. Luo, Ceram. Int. 44 (2018) 16265–16272.
[40] M. Gao, Y. Bao, Y. Qian, Y. Deng, Y. Li, G. Chen, Inorg. Chem. 57 (2018) 12245–12254.
[41] B. Chang, J. Liu, G. Qing, T. Sun, J. Mater. Chem. A 6 (2018) (1928) 11916–11928.
[42] F. Lu, Q. Chen, S. Geng, M. Allix, H. Wu, Q. Huang, X. Kuang, J. Mater. Chem. A 6 (2018) 24232–24244.
[43] L. Zhao, S. Wang, F. Pan, Z. Tang, Z. Zhang, S. Zhong, J. Zhang, J. Mater. Chem. A 6 (2018) 11688–11693.
[44] Y. Jiang, Y. Ding, P. Zhang, F. Li, Z. Yang, J. Membr. Sci. 565 (2018) 33–41.
[45] X. Zhao, H. Liu, Y. Feng, L. Pang, M. Ding, L. Deng, J. Zhu, Mater. Lett. 231 (2018) 130–133.
[46] J. Zhi, H. Cui, Z. Wang, F. Huang, Mater. Horiz. 5 (2018) 691–698.
[47] C.-S. An, B. Zhang, L.-B. Tang, B. Xiao, Z.-J. He, J.-C. Zheng, Ceram. Int. 45 (2019) 13144–13149.
[48] X. Zhao, H. Liu, M. Ding, Y. Feng, Ceram. Int. 45 (2019) 12476–12483.
[49] H. Luo, C. Xu, B. Wang, F. Jin, L. Wang, T. Liu, Y. Zhou, D. Wang, Electrochim. Acta 313 (2019) 10–19.
[50] J. Chen, E. Wang, J. Mu, B. Ai, T. Zhang, W. Ge, L. Zhang, J. Mater. Sci. 54 (2019) 592–604.
[51] B. Wang, W. Yuan, X. Zhang, M. Xiang, Y. Zhang, H. Liu, H. Wu, Inorg. Chem. 58 (2019) 8841–8853.
[52] J. Zeng, R. Jiang, H. Yu, W. Hao, X. Wen, J. Nanopart. Res. 21 (2019) 84.
[53] Y. Gao, C. Wang, P. Hu, F. He, M. Wu, H. Zhang, J. Alloys Compd. 787 (2019) 944–951.
[54] L. Wu, H. Li, X. Xie, K. Chai, P. Han, C. Zhang, C. Yang, J. Alloys Compd. 780 (2019) 482–490.
[55] C. Guo, Q. Tian, L. Yang, J. Alloys Compd. 776 (2019) 740–745.
[56] S. Li, Y. Zhang, J. Huang, J. Alloys Compd. 783 (2019) 793–800.
[57] W. Zheng, P.G. Zhang, J. Chen, W.B. Tian, Y.M. Zhang, Z.M. Sun, J. Electroanal. Chem. 835 (2019) 205–211.
[58] Z. Fu, R. Li, Z. Kan, J. Solid State Electrochem. 23 (2019) 1779–1785.
[59] X. Sun, Y. Liu, J. Zhang, L. Hou, J. Sun, C. Yuan, Electrochim. Acta 295 (2019) 237–245.
[60] F. Kong, X. He, Q. Liu, X. Qi, D. Sun, Y. Zheng, R. Wang, Y. Bai, Electrochem. Commun. 97 (2018) 16–21.
[61] S. Sun, Z. Xie, Y. Yan, S. Wu, Chem. Eng. J. 366 (2019) 460–467.
[62] C. Shen, L. Wang, A. Zhou, H. Zhang, Z. Chen, Q. Hu, G. Qin, J. Electrochem. Soc. 164 (2017) A2654–A2659.
[63] X. Li, K. Zhao, L. Zhang, Z. Ding, K. Hu, J. Alloys Compd. 692 (2017) 40–48.
[64] S.A. Mirkhani, A. Shayesteh Zeraati, E. Aliabadian, M. Naguib, U. Sundararaj, ACS Appl. Mater. Interfaces 11 (2019) 18599–18608.